Applied Surface Science 566 (2021) 150661

Contents lists available at ScienceDirect

Applied Surface Science

journal homepage: www.elsevier.com/locate/apsusc

Full Length Article

Energetic bombardment and defect generation during magnetron-sputter-deposition of metal layers on graphene

N. Pliatsikas [a], O. Karabinaki [b], M. Zarshenas [a], G.A. Almyras [a], I. Shtepliuk [a], R. Yakimova [a], J. Arvanitidis [c], D. Christofilos [b], K. Sarakinos [a,d,*]

[a] Department of Physics, Chemistry and Biology, Linköping University, Linköping, SE 581 83, Sweden
[b] School of Chemical Engineering & Physics Laboratory, Faculty of Engineering, Aristotle University of Thessaloniki, Thessaloniki, GR 54 124, Greece
[c] Physics Department, Aristotle University of Thessaloniki, Thessaloniki, GR 54 124, Greece
[d] Department of Physics, University of Helsinki, P.O. Box 64, Helsinki FI-00014, Finland

ARTICLE INFO

Keywords:
Graphene
Magnetron sputtering
Energetic bombardment
Backscattered Ar
Metal contacts

ABSTRACT

In the present work, we elucidate the interplay among energetic bombardment effects in magnetron sputtering and defect generation in two-dimensional (2D) materials. Using deposition of gold (Au) layers on single-layer graphene (SLG) as a model system, we study the effect of pressure-distance (pd) product during magnetron sputtering on the pristine SLG properties. Raman spectroscopy, complemented by X-ray photoelectron spectroscopy, shows that for pd = 8.2 Pa·cm, Au layer deposition causes defects in the SLG layer, which gradually diminish and eventually disappear with increasing pd to 82.5 Pa·cm. Stochastic and deterministic simulations of the sputtering process, the gas-phase transport, and the interaction of sputtered and plasma species with the substrate surface suggest that defects in SLG primarily emanate from ballistic damage caused by backscattered Ar atoms with energies above 100 eV. With increasing pd, and thereby gas-phase scattering, such high energy Ar species become thermalized and hence incapable of causing atomic displacements in the SLG layer. The overall results of our study suggest that control of backscattered Ar energy is a potential path toward enabling magnetron sputtering for fabrication of multifunctional metal contacts in devices founded upon 2D materials.

1. Introduction

Deposition of multifunctional metal contacts on two-dimensional (2D) materials is a key step in the fabrication of a wide array of optoelectronic, catalytic, and sensing devices [1–6]. For the performance of such devices to be optimized, metal layers (i.e., contacts) should exhibit a well-defined morphology. Moreover, control of the structure and chemistry of the metal/2D-crystal interface is also required, without substantially modifying the pristine properties of the 2D material [7–14]. Nowadays, metal layers (i.e., thin films) are routinely synthesized on 2D materials via vapor condensation using thermal or electron beam evaporation [1,15–17]. Besides vapor-based methods, wet-chemistry approaches and electroless deposition have been employed for decorating graphene-based surfaces with metal nanoparticles [18–22]. All the above-mentioned deposition strategies suffer from lack of lateral film thickness and property uniformity, while they do not provide the ability to control atomic assembly kinetics during growth; a prerequisite for tuning metal-layer morphologies and film/substrate interface properties.

Magnetron sputtering is a vapor-based deposition technique that meets the requirements of large-scale film thickness and properties uniformity, while it offers access to a wide range of process parameters for tuning growth kinetics [23]. However, it has been, up to now, deemed incompatible with metal-layer deposition on 2D materials, as it generates ample amounts of energetic neutral and ionized species, which create defects that compromise the pristine electronic and transport properties of the 2D crystals [24–31]. Hence, a fundamental understanding of the interplay among energetic bombardment effects during magnetron-sputter deposition and defect generation in 2D crystals is required for enabling magnetron sputtering in 2D-material technologies and applications.

In the present work, we contribute to the afore-mentioned understanding by studying magnetron-sputter-deposition of gold (Au) layers on single-layer-graphene (SLG). The choice of the Au/SLG model system is motivated by the fact Au is a highly inert material, suitable for contacts [3,32], while SLG offers a sensitive platform for identifying defect

* Corresponding author at: Department of Physics, Chemistry and Biology, Linköping University, Linköping, SE 581 83, Sweden.
E-mail address: kostas.sarakinos@liu.se (K. Sarakinos).

https://doi.org/10.1016/j.apsusc.2021.150661
Received 30 March 2021; Received in revised form 23 June 2021; Accepted 13 July 2021
Available online 17 July 2021

formation by spectroscopic techniques, including Raman spectroscopy [33–35]. To tune the energy of species arriving at the SLG substrate, we vary the working pressure-distance (pd) product during sputtering from 8.2 to 82.5 Pa·cm, and we deposit films with a nominal thickness of 2 nm. Morphological analysis of the film surface shows that Au grows in a pronounced three-dimensional (3D) fashion on SLG, such that only ~50% of the SLG surface is covered by the deposit at all synthesis conditions. Moreover, the increase of the pd product causes a transition from a surface that hosts partially elongated islands to a dendritic island morphology. This type of 3D morphology allows for post-deposition studies of the vibrational properties of SLG by Raman spectroscopy. Our Raman data show that deposition at pd = 8.2 Pa·cm results in considerable damage of the pristine SLG structure, which is diminished as pd increases, and effectively disorder-free growth conditions are established for pd = 82.5 Pa·cm. The Raman analysis is supported by X-ray Photoelectron Spectroscopy (XPS) measurements, which show that the fraction of sp^2 bonded carbon atoms in the substrate decreases with decreasing the pd value, i.e., smaller pd products favor the formation of defect-related structures.

Seeking to establish an atomistic understanding of the phenomenological correlations between deposition parameters and SLG properties observed in our experiments, we employ Monte Carlo (MC) simulations for estimating the energies of plasma species (sputtered Au and backscattered Ar) arriving at the SLG surface. We find that at pd = 8.2 Pa·cm, Au and Ar species exhibit broad energy distributions extending up to ~100 and ~200 eV, respectively, which become thermalized for pd = 82.5 Pa·cm. Gas-phase transport MC simulations are coupled with Classical Molecular Dynamics (CMD) to model the interactions of energetic species with SLG. CMD data show that point defects in the SLG network are primarily caused by backscattered Ar with energies above 100 eV, which is consistent with the gradual disappearance of defect related modes in the Raman spectra of Au/SLG heterostructures as pd values are increased. The overall results of this study provide knowledge for optimizing energetic input to the substrate during magnetron sputtering, such that strategies for the non-invasive growth of metal layers on 2D materials can be developed.

2. Research methodology

2.1. Film synthesis and characterization

Gold (Au) layers (i.e., thin films), with a nominal thickness of 2 nm, are grown by direct current magnetron sputtering (dcMS) on single-layer-graphene (SLG) synthesized by chemical vapor deposition on copper (Cu) substrates. It should be noted that films are deposited directly on SLG/Cu, i.e., graphene is not transferred, to avoid defect formation and explicitly study the effect of the sputtering process on the pristine graphene structure. Depositions are carried out in an ultra-high vacuum chamber (based pressure ~ 10^{-8} Pa) using argon (Ar) as a sputtering gas (gas purity 99.999%). The magnetron source, equipped with an Au target (diameter 7.62 cm, purity 99.99%), is placed at a distance d = 12.5 cm from the substrate, and at an angle of 45° with respect to the substrate surface normal. To tune the energy of the species arriving at the substrate, the working pressure p is varied in the range 0.6 to 6.7 Pa yielding pressure-distance (pd) products between 8.2 and 82.5 Pa·cm. In the remainder of the article, we present and discuss results with reference to pd (instead of p), since pd is a universal and deposition-geometry-independent parameter describing gas-phase scattering, and its effect on particle transport [36] and energy of species arriving at the substrate [37]. Ar discharges are operated at a constant current mode, and the deposition rate is held at ~0.1 Å·s^{-1} by increasing the target current density from 0.13 to 0.8 mA·cm^{-2} (corresponding to target current 6 to 37 mA) as pd is increased from 8.2 to 82.5 Pa·cm. The deposition rate at the various conditions is determined from *in situ* spectroscopic ellipsometry [38] by measuring the thickness of continuous films grown on silicon (1 0 0) substrates covered with a 530 nm thick, thermally grown, silicon dioxide overlayer [39].

The effect of sputtering conditions on the film morphology is investigated by scanning electron microscopy (SEM). Top-view images are collected using a LEO-Zeiss (1550 Gemini) Field Emission Gun SEM at an operating voltage of 4 kV. At the nominal thickness of 2 nm, the film is expected to feature isolated islands and/or clusters [40–44]. Hence, SEM data are analyzed using the ImageJ freeware [45] to determine the fraction q of the SLG surface covered by islands, as well as to define the island number densities, from which we extract the mean island projected size (MS). We also quantify the island shape by approximating the islands with ellipsoids and computing the in-plane aspect ratio (AR), i.e., the ratio of the major to the minor ellipse axis on the substrate plane.

Raman spectroscopy is employed to identify disorder in the sp^2-network of graphene at the various deposition conditions by recording changes in the characteristic D, G, and 2D Raman bands [46–51]. Raman spectra, averaged from areas 10 × 10 μm^2, are recorded using a LabRam HR micro-spectrometer (HORIBA) equipped with a Peltier-cooled charge coupled device detector. We use the 514 nm line of a diode-pumped solid-state laser, the 633 nm line of a He-Ne laser, and the 785 nm line of a diode laser as excitation wavelengths, which are focused on the sample by means of a standard 100 × objective lens. The laser power applied on the sample is kept at 0.1 (514 nm laser), 0.4 (633 nm laser), and 3.5 mW (785 nm laser) to avoid laser-heating-induced changes of the SLG properties and the Au morphology. The spectrometer is calibrated using a Si wafer and/or a Ne lamp.

Raman analysis is complemented by X-ray Photoelectron Spectroscopy (XPS). Photoelectron spectra are recorded in a Kratos AXIS Ultra DLD UHV system (base pressure ~ 10^{-8} Pa), equipped with a monochromated aluminum Kα X-ray beam (hv = 1486.6 eV), a hemispherical sector analyzer, and a multichannel detector. A 20 eV pass energy, resulting in a full width at half maximum (FWHM) for the Ag-$3d_{5/2}$ peak of less than 500 meV with a step size of 0.1 eV, is used in order to obtain information from the core-level spectra. XPS data are analyzed using the Kratos Vision software and the build-in relative sensitivity factors.

2.2. Simulations

To estimate the energy of species arriving at the substrate, we use Monte-Carlo simulations for modeling the sputtering process and the interaction of species generated at the target with Ar gas *en route* to the substrate. The sputtering of a 4 mm thick Au target by 400 eV Ar^+ ions (the Ar^+ ion energy corresponds to the typical target voltage of 400 V in our experiments) is modeled using the SRIM (Surface and Range of Ions in Matter) software package [52,53]. Besides the energy distribution of sputtered Au atoms, we also use SRIM to extract the distribution of backscattered Ar particles. Such backscattered particles may constitute a considerable fraction of the total energetic flux to the substrate, most notably in the case of large ion-target mass mismatch [54,55]. The data obtained from SRIM simulations, along with the deposition chamber geometry, are used as input for modeling the transport of species through the gas phase via the SIMTRA software package [56]. Simulations are performed for pd products consistent with experiments (see Section 2.1), while the interaction of target-emanating particles (i.e., sputtered Au and backscattered Ar) with Ar gas is described using a screened Coulomb potential with Moliére screening function [56,57]. The SIMTRA simulations yield energy distributions of sputtered Au and backscattered Ar species impinging on the substrate. These distributions guide classical molecular dynamics (CMD) simulations of the interactions of the energetic species with the SLG/Cu substrate. The above-described simulation strategy is schematically illustrated in Fig. 1.

The CMD simulations are carried out in the framework of the LAMMPS [58] freeware. The C-C interaction in the SLG layer is modeled using the adaptive intermolecular reactive bond order (AIREBO) potential by Stuart *et al.* [59], which has been successfully used in the

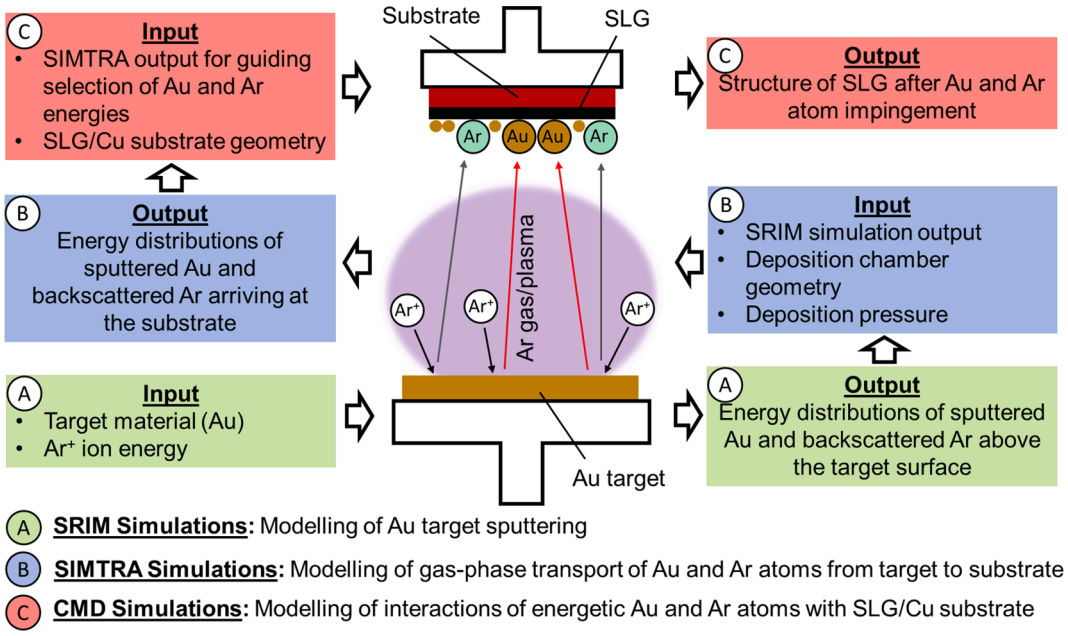

Fig. 1. Schematic illustration of the simulation strategy used in the present work. Monte-Carlo simulations (implemented within the SRIM and SIMTRA software packages) are used for modeling sputtering of Au target by Ar^+ ions (A), and gas-phase transport of sputtered Au and backscattered Ar particles through the Ar gas (B). The Monte-Carlo simulations from steps (A) and (B) yield energy distributions for Au and Ar particles arriving at the substrate, which are used to guide classical molecular dynamics (CMD) simulations (C) for modeling interactions of energetic sputtered and backscattered species with the SLG/Cu substrate.

literature to simulate ion-irradiation-induced damage in graphene [60,61]. Au-C, Ar-C, and Ar-Ar interactions are described by the Ziegler–Biersack–Littnark (ZBL) potential [52], which is a universal repulsive formalism widely used for modeling the collisions between energetic species and carbon-based materials [60,62,63]. The C-Cu interaction at the SLG/Cu interface is described using the Lennard–Jones (LJ) potential with its parameters taken from Refs. [64,65], while Cu-Cu, Au-Au, and Au-Cu interactions are modeled using the Finnis-Sinclair interatomic potential developed by Ackland *et al.* [66].

Simulations are performed using a Cu fcc substrate consisting of 24,192 atoms in an $8 \times 8 \times 4.5$ nm^3 box with the z-axis oriented along that (1 1 1) direction. In this configuration, the substrate consists of 21 atomic layers, which suffice for avoiding forward sputtering during impingement of energetic Au and Ar species. The bottommost four layers of the Cu slab are frozen to describe the bulk of the substrate. The next 12 layers are kept at a constant temperature of 300 K using a Langevin thermostat, while the topmost five layers along with SLG (consisting of 2508 C atoms) and impinging Au and Ar atoms constitute the reaction zone. Periodic boundary conditions are applied in the x and y directions, while the SLG/Cu(1 1 1) system is relaxed at the temperature of 300 K prior to impingement of Au and Ar atoms.

Arrival and impingement of energetic species at and on the SLG/Cu substrate are simulated by releasing pulses of 10 Ar or Au atoms (the time between each pulse is 50 ps) at distances between 20 and 40 Å above the substrate surface. The species are given initial velocities toward the substrate surface corresponding to energies up to 175 eV, consistent with the energies predicted by the SRIM/SIMTRA simulations (see Section 3 for more information). We use an adaptive time step of up to 0.25 fs. After arrival of the last particle pulse, the simulated systems are let to relax, and runs are completed when the temperature reaches 300 K and no considerable changes in the SLG/Cu structure are observed. The simulation output is visualized using Visual Molecular Dynamics software [67]. A schematic representation of the simulation system and representative snapshots before and after particle impingement as shown in Fig. S1 in the Supporting Information. The effect of energetic species on SLG/Cu substrate is quantified by calculating the broken and newly-created bonds in the SLG layer after particle impingement, as explained in Section S.1 and Fig. S2 in the Supporting Information.

3. Results and discussion

Fig. 2(a–d) display top-view SEM images of 2 nm Au films deposited on SLG/Cu substrates at various pd values. For pd = 8.2 Pa·cm (Fig. 2 (a)), the film surface features isolated and partially elongated islands with areal coverage q of ~51%. Increase of pd to 16.5 Pa·cm (Fig. 2(b)) yields islands that have more elongated shapes and a slight decrease of the q value to ~49.5%. By further increasing pd to 41.2 Pa·cm (Fig. 2 (c)), the islands become larger, obtain dendritic shapes, and the substrate areal coverage becomes q ≈ 49%. At the maximum pd value of 82.5 Pa·cm, (Fig. 2(d)), the island shapes remain dendritic and q decreases further to ~46%. The evolutions of the island projected size, MS and their in-plane aspect ratio, AR vs. pd are also plotted in Fig. 2(e and f), respectively, to better demonstrate that the islands become larger and their shape more elongated by increasing the sputtering pressure.

The data presented in Fig. 2 show that Au grows in a 3D fashion on SLG under all process conditions, since a significant fraction of the substrate surface remains exposed after depositing 2 nm (corresponding to ~ 10 monolayers) of material. This growth behavior is typical for weakly-interacting film/substrate systems [40,41,68–73], and it is consistent with the significantly smaller free surface energy of SLG (0.046 mJ/m^2) [74,75] relative to Au (1.5 J/m^2) [76]. Moreover, the tendency of Au islands to exhibit dendritic shapes at relatively large pd values is an indication that the increase of the gas-phase scattering frequency (caused by the increase of pd) results in a smaller amount of energy transferred from the plasma particles to the film-forming species, such that their effective diffusion length is reduced. A more detailed discussion on the correlation between pd and the energy of species arriving at the substrate is provided later in the present section.

The effect of film growth conditions on the vibrational properties of the underlying SLG substrate is demonstrated in Fig. 3, which plots Raman spectra from pristine SLG/Cu and from 2 nm thick Au/SLG/Cu samples, whereby Au layers are grown at various pd values. Spectra measured with the excitation laser wavelength of 514 nm are presented,

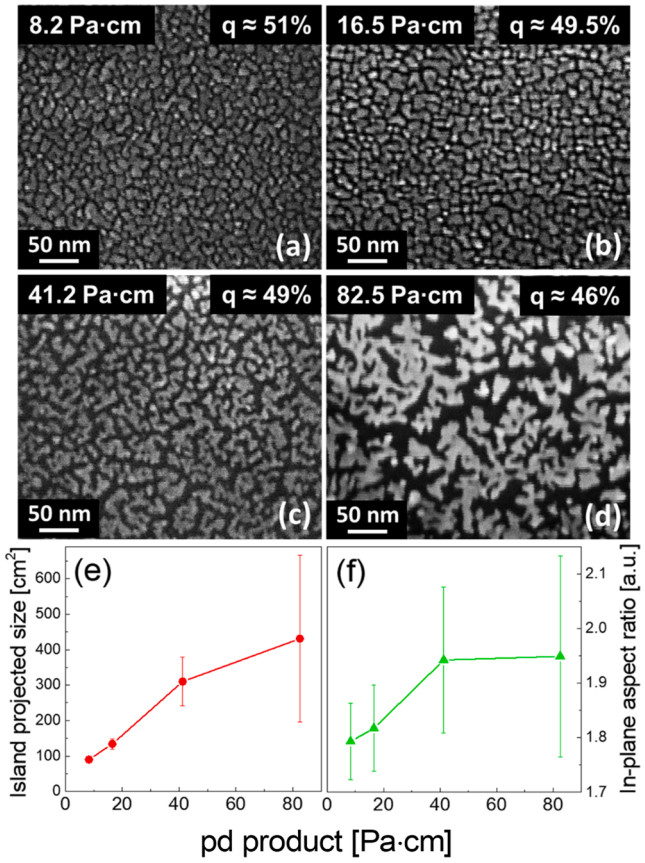

Fig. 2. Top-view SEM images of sputter-deposited 2 nm thick Au layers on SLG/Cu for pd product values of (a) 8.2 Pa·cm, (b) 16.5 Pa·cm, (c) 41.2 Pa·cm, and (d) 82.5 Pa·cm. Panels (e) and (f) plot the evolution of the island size MS and the in-plane aspect ratio AR vs. pd, whereby the standard error of both quantities is represented by error bars.

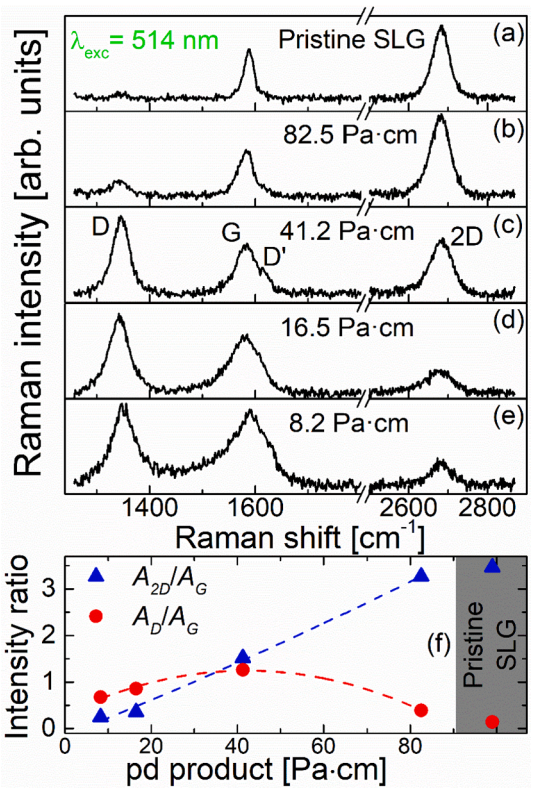

Fig. 3. Raman spectra (recorded with an excitation wavelength of 514 nm) from (a) pristine SLG and (b)-(e) SLG after 2 nm Au deposition for various pd values. (f) Integrated intensity ratios A_{2D}/A_G and A_D/A_G (extracted from the spectra in panels (a) through (e)) as a function of pd.

since this is the most widely used wavelength in the literature. The pristine SLG/Cu spectrum (Fig. 3(a)) exhibits peaks at ~1585 and ~2680 cm^{-1}, which correspond to the first-order G and the second-order 2D band of graphene, respectively [33]. In all other spectra recorded from Au decorated SLG/Cu samples (Fig. 3(b–e)) we observe: (i) an additional peak at ~1345 cm^{-1}, which can be assigned to the D band; and (ii) a shoulder on the high-frequency side of the G peak at ~1620 cm^{-1}, which corresponds to the D́ phonon mode [33]. Both afore-mentioned features in the Raman spectra in Fig. 3(b–e) indicate that deposition of Au causes the formation of defects in the graphene structure [33]. With decreasing pd, the intensity of the D peak and the widths of the D, G, and 2D peaks increase, indicating an increase in the defect density. Moreover, we find that at pd = 82.5 Pa·cm (Fig. 3(b)), the D and D́ peaks nearly disappear, i.e., close to defect-free film deposition conditions are established.

To represent quantitatively the effect of Au-layer deposition conditions on the vibrational properties and structural quality of the SLG layer, we calculate the integrated intensity ratios A_{2D}/A_G and A_D/A_G of the peaks observed in Fig. 3(a–e), and we plot those ratios as a function of pd in Fig. 3(f). For pristine SLG/Cu, we obtain a ratio $A_{2D}/A_G = 3.46$, which is close to the values for monolayer graphene reported in the literature under the same excitation conditions [77–79]. The deleterious effect of relatively low sputtering pressures for the pristine graphene properties is reflected by the monotonic decrease of A_{2D}/A_G ratio from 3.27 at pd = 82.5 Pa·cm to 0.24 at pd = 8.2 Pa·cm. The A_D/A_G ratio exhibits a more complex, non-monotonic behavior as a function of pd; it increases with increasing pd up to 41.2 Pa·cm, above which it decreases. Such behavior has been reported in the literature, and it has been attributed to the transformation from a defective to a highly-disordered carbon (graphite and graphene) structure upon increasing defect density [51,80]. Qualitatively consistent trends with regards to the integrated intensity ratios of the Raman peaks are also observed in spectra recorded with excitation wavelengths at 633 and 785 nm, see Fig. S3 (Section S.2) in the Supporting Information.

Further insights into the effect of Au deposition on the SLG/Cu properties are obtained by XPS measurements. Fig. 4(a) shows the high-resolution C-1 s core level spectrum of an Au/SLG/Cu sample, whereby the Au layer is deposited at pd = 41.2 Pa·cm. The spectrum reveals the existence of two main peaks, centered at binding energies ~289 and ~285 eV. Detailed analysis, using a Shirley background, shows that the two-peak structure can be deconvoluted into four components attributed to the sp^2 carbon bonds of graphene (binding energy 284.6 eV [81,82]), C—O and C═O bonds from surface contamination (binding energy 286.5 eV and 288.5 eV [83], respectively), defect-related sp^3 bonds (binding energy 285.2 eV [84–90]). Qualitatively similar features in the C-1s core level spectra are observed for samples grown at all deposition conditions, as well as in spectra recorded from pristine SLG/Cu substrates, as shown in Fig. S4 in the Supporting Information (Section S.3). Based on the data presented in Fig. 4(a) and S4, we plot in Fig. 4(b) the integrated intensity ratio of the sp^3-to-sp^2 related components, as a function of pd. The plot shows that the ratio decreases with increasing pd and asymptotically approaches that of pristine SLG/Cu, which is consistent with the Raman data in Figs. 3 and S3.

The experimental data presented in Figs. 3 and 4 show that the pd parameter has a pronounced effect on the structural quality of graphene, whereby decrease of pd yields a larger density of defects. It is also known that the pd product determines the frequency of collisions in the gas phase and, thereby, the energy of species arriving at the substrate during film growth. We quantify this effect by combining SRIM and SIMTRA simulations to determine the energy distributions of Au and Ar at the

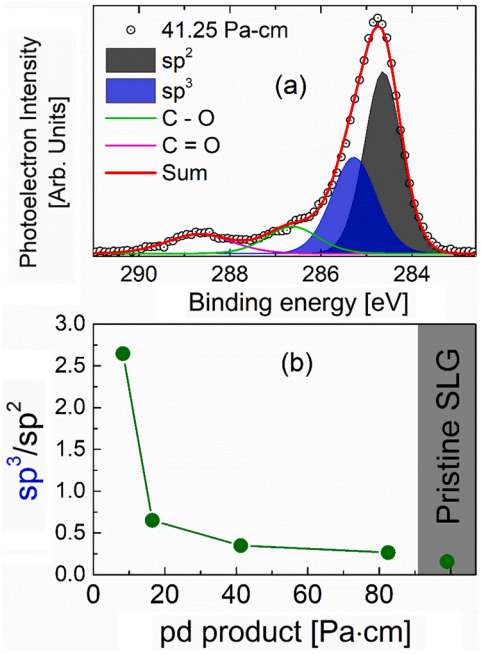

Fig. 4. (a) XPS C-1 s spectra of 2 nm Au deposited on SLG/Cu at pd = 41.2 Pa·cm. Open circles represent the experimental spectrum, black, blue, green, and magenta lines represent the individual fitting components, while their sum is represented by the red line. (b) The sp^3/sp^2 ratio, calculated from the blue and black components, respectively, as a function of pd.

substrate position for the various deposition conditions (see Section 2.2. for details), which are plotted in Fig. 5. For pd = 8.2 Pa·cm, both Au and Ar species exhibit broad energy distributions (Fig. 5(a) and (e), respectively) with tails extending up to ~200 eV. However, the distribution of Ar is more uniform resulting in a mean energy E_{mean} of 23.4 eV, as opposed to the distribution of Au which decays strongly as function of energy, yielding E_{mean} = 4 eV. With increasing pd, the energy distributions of both species become narrower and E_{mean} decreases until monoenergetic thermalized fluxes with E_{mean} = 0.04 eV are obtained for pd = 82.5 Pa·cm (Fig. 5(d) and (h)).

The data presented in Fig. 5 indicate that for pd values 8.2 and 16.5 Pa·cm the substrate is subjected to bombardment by species having a wide range of energies, such that defect formation in SLG may be the result of all energetic contributions. Designing CMD simulations to account for and model the simultaneous arrival of all species (Au and Ar) on SLG/Cu, with energies and relative fluxes consistent with the distributions in Fig. 5, is a non-trivial task. Instead, we chose here to study the effect of each species and energy represented in the data in Fig. 5 separately and assess their propensity to cause defects in SLG. To this purpose, we simulate by CMD the impingement of Au and Ar atoms with energies exhibiting relative statistical frequencies down to 10^{-3} in their respective distributions, i.e., up to 90 eV for Au and 175 eV for Ar. The results show that Au atoms with energies up to 50 eV cause no defect formation in the SLG layer. Increase of the Au projectile energy to 90 eV leads to the appearance of Stone-Wales defects [91], i.e., C atoms are rearranged in a way that four neighboring hexagonal rings are transformed into two pentagons and two heptagons (see Fig. 6(a)). With regards to backscattered Ar species, the simulation data show that the Ar species with energies below 100 eV have no effect on the SLG structure, while their effect becomes more pronounced at energies 110 eV and above. For impinging energies in the range 110–130 eV, Ar atoms cause transformation of the hexagons into pentagons, heptagons and nonagons (see Fig. 6(b)). Increasing the Ar atoms energy above 130 eV yields sputter-removal of carbon atoms from the SLG and the formation of vacancies (Fig. 6(c)). All type of bombardment-induced defects evidenced in the CMD simulations are consistent with the appearance of clear D and Ď peaks in the Raman spectra (Figs. 3 and S3) and sp^3 components in the XPS spectra (Figs. 4 and S4) for samples grown at pd < 82.5 Pa·cm [34,92–94].

To further assess the extent of the damage caused by Ar atoms (irrespective of the type of defect), we use the CMD data to compute and present in Fig. 7 the ratio $\frac{\sum N_{bb}}{\sum N_{C-C}}$ of the total number of broken C-C bonds

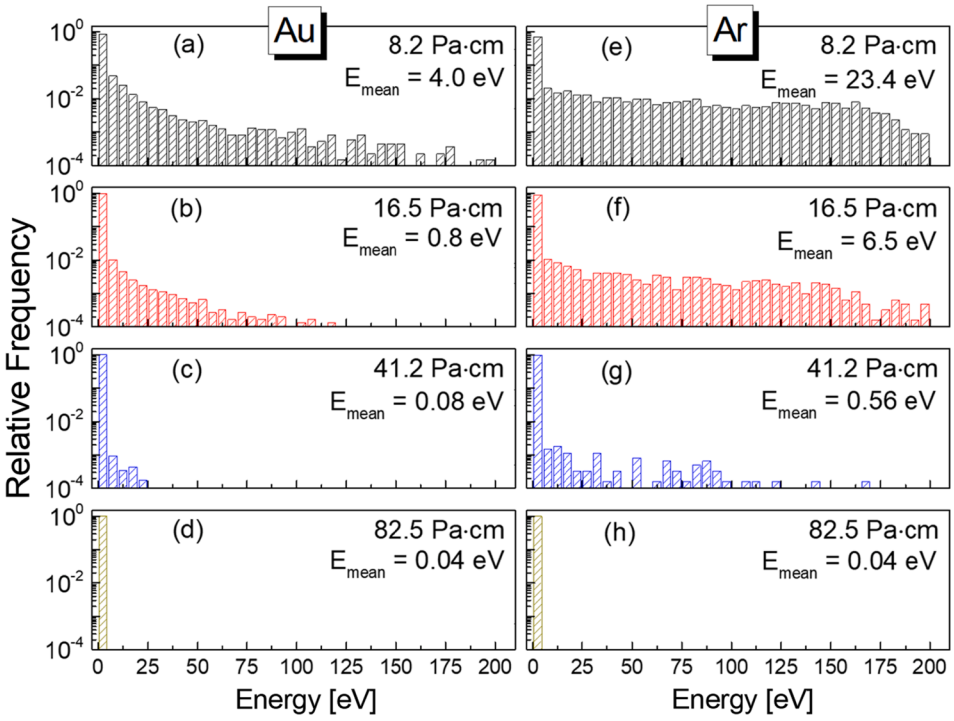

Fig. 5. Energy distributions of (a) – (d) sputtered Au and (e) – (h) backscattered Ar species impinging on the substrate, as determined by SRIM and SIMTRA simulations. Simulations are performed for pd products from 8.2 to 82.5 Pa·cm to be consistent with the experiments.

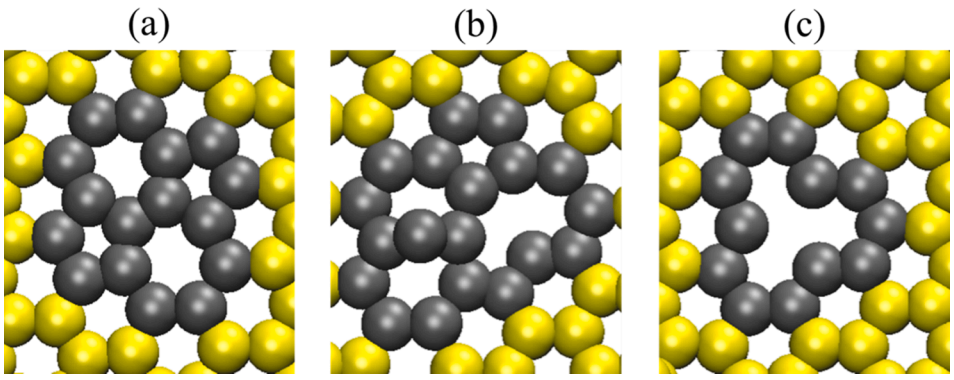

Fig. 6. CMD simulation snapshots representing the most common types of defects observed in the SLG layer upon energetic atom (Au or Ar) impingement. The defects are marked with gray spheres. (a) Four hexagons are transformed into two pentagons and two heptagons (Stone-Wales defect), caused by Au atoms with energies of ~ 90 eV. (b) Four hexagons are transformed into one pentagon, two heptagons and one nonagon, typically caused by Ar atoms with energies in the range 110 to 130 eV. (c) Three hexagons are transformed into one dodecagon, which is caused by the removal of a carbon atom (single vacancy), typically caused for Ar atoms with energies in the range 130 to 175 eV.

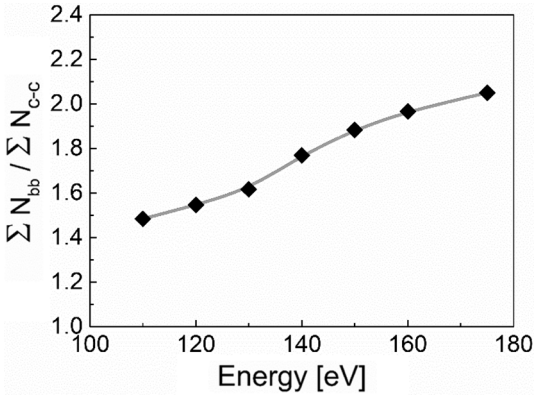

Fig. 7. Ratio of broken to newly-formed C-C bonds $\frac{\sum N_{bb}}{\sum N_{C-C}}$ in SLG, as a function of the energy of impinging Ar atoms, extracted from CMD simulation data.

(N_{bb}) to the total number of new Carbon-Carbon bonds ($N_{C\text{-}C}$) formed after Ar atom impingement and relaxation, as a function of the impingement energy (see Section S.1 in the Supporting Information for details with regards to the $\frac{\sum N_{bb}}{\sum N_{C-C}}$ ratio calculation). We note again that for energies below 110 eV no defects are formed and hence no $\frac{\sum N_{bb}}{\sum N_{C-C}}$ values are computed. The data show that $\frac{\sum N_{bb}}{\sum N_{C-C}}$ increases monotonically with Ar atom energy, which can be interpreted as an increase in the defect density. The overall results of the CMD simulations suggest that the majority of defects in SLG in our deposition process primarily emanate from ballistic damage caused by Ar atoms with energies above 100 eV. Moreover, the sputtering and gas-phase transport simulations (SRIM and SIMTRA, respectively) show that the flux of defect-causing Ar atoms gradually diminishes and eventually disappears with increasing sputtering pressure. This can explain the nearly defect-free SLG structure observed in the Raman and XPS data for films grown at pd = 82.5 Pa·cm. We also note that Ar gas heating and rarefaction [95,96] —caused from collisions between sputtered Au and gas Ar atoms— is unlikely to have a pronounced effect on the transport and mean energy of species arriving at the substrate, due to the relatively small discharge currents (6–37 mA, see Section 2.2 for details) used in our experiments.

4. Summary and outlook

We present a systematic study on the effect of magnetron-sputter-deposited gold (Au) layers (i.e., thin films) on the structural integrity of single-layer graphene (SLG). Films with a nominal thickness of 2 nm are deposited for pressure-distance (pd) products in the range 8.2 to 82.5 Pa·cm. Analysis of the SLG vibrational modes (probed by means of Raman spectroscopy), complemented by X-ray photoelectron spectroscopy measurements, show that film deposition at pd = 8.2 Pa·cm results in formation of defects in the graphene substrate. This deleterious effect is diminished with increasing pd values, and a nearly defect-free SLG structure is achieved when depositing at pd = 82.5 Pa·cm. Seeking understand the atomistic origin of this behavior, we employ Monte-Carlo and classical molecular dynamics simulations to model the processes of sputtering, gas-phase transport, and impingement of sputtering-related species on the substrate. The simulation data show that defects in SLG primarily originate from ballistic damage caused by energetic Ar species that are backscattered at the target surface and arrive at the substrate with energies above 100 eV. With increasing pd, gas-phase scattering causes the gradual thermalization of high-energy species, such that no atomic rearrangement and defect generation occurs at pd = 82.5 Pa·cm. Our overall results highlight a potential path, e.g., by using complex pd patterns, for enabling sputtering in the synthesis of metal contacts on graphene and other 2D materials, which is a key step toward industrial-scale fabrication of key enabling devices.

CRediT authorship contribution statement

N. Pliatsikas: Conceptualization, Methodology, Formal analysis, Investigation, Writing – original draft. **O. Karabinaki:** Formal analysis, Investigation, Writing - review & editing. **M. Zarshenas:** Methodology, Formal analysis, Investigation, Writing - review & editing. **G.A. Almyras:** Methodology, Writing - review & editing. **I. Shtepliuk:** Conceptualization, Writing - review & editing. **R. Yakimova:** Conceptualization, Writing - review & editing. **J. Arvanitidis:** Conceptualization, Methodology, Formal analysis, Investigation, Writing - review & editing, Supervision. **D. Christofilos:** Conceptualization, Methodology, Formal analysis, Investigation, Writing - review & editing, Supervision, Funding acquisition. **K. Sarakinos:** Conceptualization, Methodology, Writing - review & editing, Supervision, Funding acquisition.

Declaration of Competing Interest

The authors declare that they have no known competing financial interests or personal relationships that could have appeared to influence the work reported in this paper.

Acknowledgements

KS acknowledges financial support from Linköping University ("LiU Career Contract, Dnr-LiU-2015-01510, 2015–2020"), the Swedish research council (contract VR-2015-04630), and the Åforsk foundation (contract ÅF 19-137). KS, NP, and MZ acknowledge financial support from the Olle Engkvist foundation (contract SOEB 190-312). KS and NP acknowledge financial support from the Wenner-Gren foundations (contracts UPD2018-0071 and UPD2019-0007). OK, JA and DC acknowledge the Center for Interdisciplinary Research and Innovation

of the Aristotle University of Thessaloniki (CIRI-AUTH) for the use of the Raman instrumentation.

Appendix A. Supplementary material

Supplementary data to this article can be found online at https://doi.org/10.1016/j.apsusc.2021.150661.

References

[1] M. Politou, I. Asselberghs, I. Radu, T. Conard, O. Richard, C.S. Lee, K. Martens, S. Sayan, C. Huyghebaert, Z. Tokei, S. De Gendt, M. Heyns, Transition metal contacts to graphene, Appl. Phys. Lett. 107 (15) (2015) 153104, https://doi.org/10.1063/1.4933192.

[2] T. Cusati, G. Fiori, A. Gahoi, V. Passi, M.C. Lemme, A. Fortunelli, G. Iannaccone, Electrical properties of graphene-metal contacts, Sci. Rep. 7 (2017) 5109, https://doi.org/10.1038/s41598-017-05069-7.

[3] X. Liu, C.-Z. Wang, M. Hupalo, H.-Q. Lin, K.-M. Ho, M. Tringides, Metals on Graphene: Interactions, Growth Morphology, and Thermal Stability, Crystals. 3 (2013) 79–111, https://doi.org/10.3390/cryst3010079.

[4] Y. Wang, J.C. Kim, R.J. Wu, J. Martinez, X. Song, J. Yang, F. Zhao, A. Mkhoyan, H. Y. Jeong, M. Chhowalla, Van der Waals contacts between three-dimensional metals and two-dimensional semiconductors, Nature. 568 (7750) (2019) 70–74, https://doi.org/10.1038/s41586-019-1052-3.

[5] K. Xu, Z. Zhao, X. Wu, W. Zhu, Van der Waals metallic alloy contacts for multifunctional devices, 2D Mater. 7 (2) (2020) 025035, https://doi.org/10.1088/2053-1583/ab734d.

[6] A. Di Bartolomeo, Graphene Schottky diodes: An experimental review of the rectifying graphene/semiconductor heterojunction, Phys. Rep. 606 (2016) 1–58, https://doi.org/10.1016/j.physrep.2015.10.003.

[7] B. Xia, Q. Guo, D. Gao, S. Shi, K. Tao, High temperature ferromagnetism in Cu-doped MoS 2 nanosheets, J. Phys. D. Appl. Phys. 49 (16) (2016) 165003, https://doi.org/10.1088/0022-3727/49/16/165003.

[8] L. Li, X. Chen, C.-H. Wang, J.i. Cao, S. Lee, A. Tang, C. Ahn, S. Singha Roy, M. S. Arnold, H.-S. Wong, Vertical and Lateral Copper Transport through Graphene Layers, ACS Nano. 9 (8) (2015) 8361–8367, https://doi.org/10.1021/acsnano.5b03038.

[9] C. Qiu, H. Zhou, B. Cao, L. Sun, T. Yu, Raman spectroscopy of morphology-controlled deposition of Au on graphene, Carbon N. Y. 59 (2013) 487–494, https://doi.org/10.1016/j.carbon.2013.03.043.

[10] D. Jing, A. Lii-Rosales, K.C. Lai, Q. Li, J. Kim, M.C. Tringides, J.W. Evans, P. A. Thiel, Non-equilibrium growth of metal clusters on a layered material: Cu on MoS 2, New J. Phys. 22 (5) (2020) 053033, https://doi.org/10.1088/1367-2630/ab84b5.

[11] T. Shen, D. Valencia, Q. Wang, K.-C. Wang, M. Povolotskyi, M.J. Kim, G. Klimeck, Z. Chen, J. Appenzeller, MoS 2 for Enhanced Electrical Performance of Ultrathin Copper Films, ACS Appl. Mater. Interfaces. 11 (31) (2019) 28345–28351, https://doi.org/10.1021/acsami.9b0338110.1021/acsami.9b03381.s001.

[12] L.i. Liu, Z. Chen, L. Wang, E. Polyakova (Stolyarova), T. Taniguchi, K. Watanabe, J. Hone, G.W. Flynn, L.E. Brus, Slow Gold Adatom Diffusion on Graphene: Effect of Silicon Dioxide and Hexagonal Boron Nitride Substrates, J. Phys. Chem. B. 117 (16) (2013) 4305–4312, https://doi.org/10.1021/jp305521g.

[13] Z. Luo, L.A. Somers, Y. Dan, T. Ly, N.J. Kybert, E.J. Mele, A.T.C. Johnson, Size-Selective Nanoparticle Growth on Few-Layer Graphene Films, Nano Lett. 10 (3) (2010) 777–781, https://doi.org/10.1021/nl9026605.

[14] H. Zhou, C. Qiu, F. Yu, H. Yang, M. Chen, L. Hu, L. Sun, Thickness-Dependent Morphologies and Surface-Enhanced Raman Scattering of Ag Deposited on n -Layer Graphenes, J. Phys. Chem. C. 115 (23) (2011) 11348–11354, https://doi.org/10.1021/jp112421q.

[15] I. Serrano-Esparza, J. Fan, J.M. Michalik, L.A. Rodríguez, M.R. Ibarra, J.M. de Teresa, The nature of graphene–metal bonding probed by Raman spectroscopy: the special case of cobalt, J. Phys. D. Appl. Phys. 49 (10) (2016) 105301, https://doi.org/10.1088/0022-3727/49/10/105301.

[16] T. Le Quang, L. Huder, F. Lipp Bregolin, A. Artaud, H. Okuno, N. Mollard, S. Pouget, G. Lapertot, A.G.M. Jansen, F. Lefloch, E.F.C. Driessen, C. Chapelier, V. T. Renard, Epitaxial electrical contact to graphene on SiC, Carbon N. Y. 121 (2017) 48–55, https://doi.org/10.1016/j.carbon.2017.05.048.

[17] C. Gong, D. Hinojos, W. Wang, N. Nijem, B. Shan, R.M. Wallace, K. Cho, Y. J. Chabal, Metal–Graphene–Metal Sandwich Contacts for Enhanced Interface Bonding and Work Function Control, ACS Nano. 6 (6) (2012) 5381–5387, https://doi.org/10.1021/nn301241p.

[18] A.M. Zaniewski, C.J. Trimble, R.J. Nemanich, Modifying the chemistry of graphene with substrate selection: A study of gold nanoparticle formation, Appl. Phys. Lett. 106 (12) (2015) 123104, https://doi.org/10.1063/1.4916567.

[19] A. Gutés, C. Carraro, R. Maboudian, Single-layer CVD-grown graphene decorated with metal nanoparticles as a promising biosensing platform, Biosens. Bioelectron. 33 (1) (2012) 56–59, https://doi.org/10.1016/j.bios.2011.12.018.

[20] T.T. Baby, S.S.J. Aravind, T. Arockiadoss, R.B. Rakhi, S. Ramaprabhu, Metal decorated graphene nanosheets as immobilization matrix for amperometric glucose biosensor, Sensors Actuat. B Chem. 145 (1) (2010) 71–77, https://doi.org/10.1016/j.snb.2009.11.022.

[21] I.V. Lightcap, T.H. Kosel, P.V. Kamat, Anchoring Semiconductor and Metal Nanoparticles on a Two-Dimensional Catalyst Mat. Storing and Shuttling Electrons with Reduced Graphene Oxide, Nano Lett. 10 (2) (2010) 577–583, https://doi.org/10.1021/nl9035109.

[22] W. Hong, H. Bai, Y. Xu, Z. Yao, Z. Gu, G. Shi, Preparation of Gold Nanoparticle/Graphene Composites with Controlled Weight Contents and Their Application in Biosensors, J. Phys. Chem. C. 114 (4) (2010) 1822–1826, https://doi.org/10.1021/jp9101724.

[23] D. Depla, S. Mahieu, J.E. Greene, Sputter Deposition Processes, in: Handb. Depos. Technol. Film. Coatings, Elsevier, 2010, pp. 253–296. https://doi.org/10.1016/B978-0-8155-2031-3.00005-3.

[24] X.P. Qiu, Y.J. Shin, J. Niu, N. Kulothungasagaran, G. Kalon, C. Qiu, T. Yu, H. Yang, Disorder-free sputtering method on graphene, AIP Adv. 2 (3) (2012) 032121, https://doi.org/10.1063/1.4739783.

[25] C. Zhang, W. Zhao, K. Bi, J. Ma, J. Wang, Z. Ni, Z. Ni, Y. Chen, Heat conduction across metal and nonmetal interface containing imbedded graphene layers, Carbon N. Y. 64 (2013) 61–66, https://doi.org/10.1016/j.carbon.2013.07.021.

[26] G. Cheng, I. Calizo, A.R. Hight Walker, Metal-catalyzed etching of graphene governed by metal–carbon interactions: A comparison of Fe and Cu, Carbon N. Y. 81 (2015) 678–687, https://doi.org/10.1016/j.carbon.2014.10.005.

[27] S.A. Imam, A. Guermoune, M. Siaj, T. Szkopek, Oxide and nitride encapsulation of large-area graphene field effect devices, Thin Solid Films. 520 (24) (2012) 7041–7043, https://doi.org/10.1016/j.tsf.2012.07.132.

[28] M.M. Giangregorio, M. Losurdo, G.V. Bianco, E. Dilonardo, P. Capezzuto, G. Bruno, Synthesis and characterization of plasmon resonant gold nanoparticles and graphene for photovoltaics, Mater. Sci. Eng. B. 178 (9) (2013) 559–567, https://doi.org/10.1016/j.mseb.2012.10.034.

[29] L.E.G. Armas, G.T. Landi, M.F.G. Huila, A. Champi, M. Pojar, A.C. Seabra, A. D. Santos, K. Araki, H.E. Toma, Graphene modification with gold nanoparticles using the gas aggregation technique, Diam. Relat. Mater. 23 (2012) 18–22, https://doi.org/10.1016/j.diamond.2011.12.038.

[30] H. Ago, Y. Kayo, P. Solís-Fernández, K. Yoshida, M. Tsuji, Synthesis of high-density arrays of graphene nanoribbons by anisotropic metal-assisted etching, Carbon N. Y. 78 (2014) 339–346, https://doi.org/10.1016/j.carbon.2014.07.010.

[31] J. Shen, L. Yang, K. Hu, W. Luo, G. Cheng, Rh nanoparticles supported on graphene as efficient catalyst for hydrolytic dehydrogenation of amine boranes for chemical hydrogen storage, Int. J. Hydrogen Energy. 40 (2) (2015) 1062–1070, https://doi.org/10.1016/j.ijhydene.2014.11.031.

[32] H. Zhou, F. Yu, H. Yang, M. Chen, G. Wang, L. Sun, High-throughput thickness determination of n-layer graphenes via gold deposition, Chem. Phys. Lett. 518 (2011) 76–80, https://doi.org/10.1016/j.cplett.2011.10.052.

[33] L.M. Malard, M.A. Pimenta, G. Dresselhaus, M.S. Dresselhaus, Raman spectroscopy in graphene, Phys. Rep. 473 (5-6) (2009) 51–87, https://doi.org/10.1016/j.physrep.2009.02.003.

[34] F. Banhart, J. Kotakoski, A.V. Krasheninnikov, Structural Defects in Graphene, ACS Nano. 5 (1) (2011) 26–41, https://doi.org/10.1021/nn102598m.

[35] X. Liu, Y. Han, J.W. Evans, A.K. Engstfeld, R.J. Behm, M.C. Tringides, M. Hupalo, H.-Q. Lin, L.i. Huang, K.-M. Ho, D. Appy, P.A. Thiel, C.-Z. Wang, Growth morphology and properties of metals on graphene, Prog. Surf. Sci. 90 (4) (2015) 397–443, https://doi.org/10.1016/j.progsurf.2015.07.001.

[36] T.P. Drüsedau, M. Löhmann, B. Garke, Decay length of the pressure dependent deposition rate for magnetron sputtering, J. Vac. Sci. Technol. A Vacuum, Surfaces, Film. 16 (4) (1998) 2728–2732, https://doi.org/10.1116/1.581408.

[37] A. Atiser, S. Mráz, J.M. Schneider, Pressure dependence of the Al ion energy distribution functions during filtered cathodic arc thin film growth in an Ar, O 2 ambient, J. Phys. D. Appl. Phys. 42 (1) (2009) 015202, https://doi.org/10.1088/0022-3727/42/1/015202.

[38] M. Konpan, Manipulation of thin metal film growth on weakly-interacting substrates using gaseous surfactants, Linköping University Electronic Press, Linköping, 2019. https://liu.diva-portal.org/smash/record.jsf?pid=diva2%3A1333761&dswid=8774.

[39] V. Elofsson, B. Lü, D. Magnfält, E.P. Münger, K. Sarakinos, Unravelling the physical mechanisms that determine microstructural evolution of ultrathin Volmer-Weber films, J. Appl. Phys. 116 (4) (2014) 044302, https://doi.org/10.1063/1.4890522.

[40] N. Pliatsikas, A. Jamnig, M. Konpan, A. Delimitis, G. Abadias, K. Sarakinos, Manipulation of thin silver film growth on weakly interacting silicon dioxide substrates using oxygen as a surfactant, J. Vac. Sci. Technol. A. 38 (4) (2020) 043406, https://doi.org/10.1116/6.0000244.

[41] A. Jamnig, N. Pliatsikas, M. Konpan, J. Lu, T. Kehagias, A.N. Kotanidis, N. Kalfagiannis, D.V. Bellas, E. Lidorikis, J. Kovac, G. Abadias, I. Petrov, J. E. Greene, K. Sarakinos, 3D-to-2D Morphology Manipulation of Sputter-Deposited Nanoscale Silver Films on Weakly Interacting Substrates via Selective Nitrogen Deployment for Multifunctional Metal Contacts, ACS Appl. Nano Mater. 3 (5) (2020) 4728–4738, https://doi.org/10.1021/acsanm.0c0073610.1021/acsanm.0c00736.s001.

[42] A. Jamnig, N. Pliatsikas, G. Abadias, K. Sarakinos, On the effect of copper as wetting agent during growth of thin silver films on silicon dioxide substrates, Appl. Surf. Sci. 538 (2021) 148056, https://doi.org/10.1016/j.apsusc.2020.148056.

[43] J. Colin, A. Jamnig, C. Furgeaud, A. Michel, N. Pliatsikas, K. Sarakinos, G. Abadias, In Situ and Real-Time Nanoscale Monitoring of Ultra-Thin Metal Film Growth Using Optical and Electrical Diagnostic Tools, Nanomaterials. 10 (2020) 2225, https://doi.org/10.3390/nano10112225.

[44] A. Jamnig, D.G. Sangiovanni, G. Abadias, K. Sarakinos, Atomic-scale diffusion rates during growth of thin metal films on weakly-interacting substrates, Sci. Rep. 9 (2019) 6640, https://doi.org/10.1038/s41598-019-43107-8.

[45] C.A. Schneider, W.S. Rasband, K.W. Eliceiri, NIH Image to ImageJ: 25 years of image analysis, Nat. Methods. 9 (7) (2012) 671–675, https://doi.org/10.1038/nmeth.2089.

[46] M.M. Lucchese, F. Stavale, E.H.M. Ferreira, C. Vilani, M.V.O. Moutinho, R. B. Capaz, C.A. Achete, A. Jorio, Quantifying ion-induced defects and Raman relaxation length in graphene, Carbon N. Y. 48 (5) (2010) 1592–1597, https://doi.org/10.1016/j.carbon.2009.12.057.
[47] G. Compagnini, F. Giannazzo, S. Sonde, V. Raineri, E. Rimini, Ion irradiation and defect formation in single layer graphene, Carbon N. Y. 47 (14) (2009) 3201–3207, https://doi.org/10.1016/j.carbon.2009.07.033.
[48] L.G. Cançado, A. Jorio, E.H.M. Ferreira, F. Stavale, C.A. Achete, R.B. Capaz, M.V. O. Moutinho, A. Lombardo, T.S. Kulmala, A.C. Ferrari, Quantifying Defects in Graphene via Raman Spectroscopy at Different Excitation Energies, Nano Lett. 11 (8) (2011) 3190–3196, https://doi.org/10.1021/nl201432g.
[49] C. Casiraghi, S. Pisana, K.S. Novoselov, A.K. Geim, A.C. Ferrari, Raman fingerprint of charged impurities in graphene, Appl. Phys. Lett. 91 (23) (2007) 233108, https://doi.org/10.1063/1.2818692.
[50] O. Frank, G. Tsoukleri, I. Riaz, K. Papagelis, J. Parthenios, A.C. Ferrari, A.K. Geim, K.S. Novoselov, C. Galiotis, Development of a universal stress sensor for graphene and carbon fibres, Nat. Commun. 2 (2011) 255, https://doi.org/10.1038/ncomms1247.
[51] A. Eckmann, A. Felten, A. Mishchenko, L. Britnell, R. Krupke, K.S. Novoselov, C. Casiraghi, Probing the Nature of Defects in Graphene by Raman Spectroscopy, Nano Lett. 12 (8) (2012) 3925–3930, https://doi.org/10.1021/nl300901a.
[52] J.F. Ziegler, J.P. Biersack, U. Littmark, The Stopping and Range of Ions in Matter, Springer, US, Boston, MA (1985), https://doi.org/10.1007/978-1-4615-8103-1_3.
[53] J.F. Ziegler, M.D. Ziegler, J.P. Biersack, SRIM – The stopping and range of ions in matter (2010), Nucl. Instruments Methods Phys. Res. Sect. B Beam Interact. with Mater. Atoms 268 (2010) 1818–1823, https://doi.org/10.1016/j.nimb.2010.02.091.
[54] K. Sarakinos, J. Alami, P.M. Karimi, D. Severin, M. Wuttig, The role of backscattered energetic atoms in film growth in reactive magnetron sputtering of chromium nitride, J. Phys. D. Appl. Phys. 40 (3) (2007) 778–785, https://doi.org/10.1088/0022-3727/40/3/014.
[55] I. Petrov, A. Myers, J.E. Greene, J.R. Abelson, Mass and energy resolved detection of ions and neutral sputtered species incident at the substrate during reactive magnetron sputtering of Ti in mixed Ar+N 2 mixtures, J. Vac. Sci. Technol. A Vacuum, Surfaces, Film. 12 (5) (1994) 2846–2854, https://doi.org/10.1116/1.578955.
[56] K. Van Aeken, S. Mahieu, D. Depla, The metal flux from a rotating cylindrical magnetron: a Monte Carlo simulation, J. Phys. D. Appl. Phys. 41 (20) (2008) 205307, https://doi.org/10.1088/0022-3727/41/20/205307.
[57] D. Depla, W.P. Leroy, Magnetron sputter deposition as visualized by Monte Carlo modeling, Thin Solid Films. 520 (20) (2012) 6337–6354, https://doi.org/10.1016/j.tsf.2012.06.032.
[58] S. Plimpton, Fast Parallel Algorithms for Short-Range Molecular Dynamics, J. Comput. Phys. 117 (1) (1995) 1–19, https://doi.org/10.1006/jcph.1995.1039.
[59] S.J. Stuart, A.B. Tutein, J.A. Harrison, A reactive potential for hydrocarbons with intermolecular interactions, J. Chem. Phys. 112 (14) (2000) 6472–6486, https://doi.org/10.1063/1.481208.
[60] X. Wu, H. Zhao, J. Pei, Fabrication of nanopore in graphene by electron and ion beam irradiation: Influence of graphene thickness and substrate, Comput. Mater. Sci. 102 (2015) 258–266, https://doi.org/10.1016/j.commatsci.2015.02.042.
[61] S. Wang, Q. Zhang, K. Yin, B. Gao, S. Zhang, G. Wang, H. Liu, The Influence of Copper Substrates on Irradiation Effects of Graphene: A Molecular Dynamics Study, Materials (Basel). 12 (2019) 319, https://doi.org/10.3390/ma12020319.
[62] A.V. Krasheninnikov, K. Nordlund, J. Keinonen, F. Banhart, Ion-irradiation-induced welding of carbon nanotubes, Phys. Rev. B. 66 (2002), 245403, https://doi.org/10.1103/PhysRevB.66.245403.
[63] J. Martinez-Asencio, C.J. Ruestes, E.M. Bringa, M.J. Caturla, Controlled rippling of graphene via irradiation and applied strain modify its mechanical properties: a nanoindentation simulation study, Phys. Chem. Chem. Phys. 18 (20) (2016) 13897–13903, https://doi.org/10.1039/C6CP01487A.
[64] S. Weng, H. Ning, T. Fu, N. Hu, Y. Zhao, C. Huang, X. Peng, Molecular dynamics study of strengthening mechanism of nanolaminated graphene/Cu composites under compression, Sci. Rep. 8 (2018) 3089, https://doi.org/10.1038/s41598-018-21390-1.
[65] X.J. Long, B. Li, L. Wang, J.Y. Huang, J. Zhu, S.N. Luo, Shock response of Cu/graphene nanolayered composites, Carbon N. Y. 103 (2016) 457–463, https://doi.org/10.1016/j.carbon.2016.03.039.
[66] G.J. Ackland, V. Vitek, Many-body potentials and atomic-scale relaxations in noble-metal alloys, Phys. Rev. B. 41 (15) (1990) 10324–10333, https://doi.org/10.1103/PhysRevB.41.10324.
[67] W. Humphrey, A. Dalke, K. Schulten, VMD: Visual molecular dynamics, J. Mol. Graph. 14 (1) (1996) 33–38, https://doi.org/10.1016/0263-7855(96)00018-5.
[68] B. Lü, G.A. Almyras, V. Gervilla, J.E. Greene, K. Sarakinos, Formation and morphological evolution of self-similar 3D nanostructures on weakly interacting substrates, Phys. Rev. Mater. 2 (2018), 063401, https://doi.org/10.1103/PhysRevMaterials.2.063401.
[69] V. Gervilla, G.A. Almyras, F. Thunström, J.E. Greene, K. Sarakinos, Dynamics of 3D-island growth on weakly-interacting substrates, Appl. Surf. Sci. 488 (2019) 383–390, https://doi.org/10.1016/j.apsusc.2019.05.208.
[70] B. Lü, V. Elofsson, E.P. Münger, K. Sarakinos, Dynamic competition between island growth and coalescence in metal-on-insulator deposition, Appl. Phys. Lett. 105 (16) (2014) 163107, https://doi.org/10.1063/1.4900575.
[71] X. Liu, C.Z. Wang, M. Hupalo, W.C. Lu, M.C. Tringides, Y.X. Yao, K.M. Ho, Metals on graphene: correlation between adatom adsorption behavior and growth morphology, Phys. Chem. Chem. Phys. 14 (25) (2012) 9157, https://doi.org/10.1039/c2cp40527j.
[72] X. Liu, M. Hupalo, C.-Z. Wang, W.-C. Lu, P.A. Thiel, K.-M. Ho, M.C. Tringides, Growth morphology and thermal stability of metal islands on graphene, Phys. Rev. B. 86 (2012), 081414, https://doi.org/10.1103/PhysRevB.86.081414.
[73] C.T. Campbell, Metal films and particles on oxide surfaces: structural, electronic and chemisorptive properties, J. Chem. Soc. Faraday Trans. 92 (9) (1996) 1435, https://doi.org/10.1039/ft9969201435.
[74] S. Wang, Y. Zhang, N. Abidi, L. Cabrales, Wettability and Surface Free Energy of Graphene Films, Langmuir. 25 (18) (2009) 11078–11081, https://doi.org/10.1021/la901402f.
[75] Z. Zhou, F. Gao, D.W. Goodman, Deposition of metal clusters on single-layer graphene/Ru(0001): Factors that govern cluster growth, Surf. Sci. 604 (13-14) (2010) L31–L38, https://doi.org/10.1016/j.susc.2010.03.008.
[76] F. Aqra, A. Ayyad, Surface energies of metals in both liquid and solid states, Appl. Surf. Sci. 257 (15) (2011) 6372–6379, https://doi.org/10.1016/j.apsusc.2011.01.123.
[77] A.C. Ferrari, Raman spectroscopy of graphene and graphite: Disorder, electron–phonon coupling, doping and nonadiabatic effects, Solid State Commun. 143 (1-2) (2007) 47–57, https://doi.org/10.1016/j.ssc.2007.03.052.
[78] J.S. Park, A. Reina, R. Saito, J. Kong, G. Dresselhaus, M.S. Dresselhaus, G′ band Raman spectra of single, double and triple layer graphene, Carbon N. Y. 47 (2009) 1303–1310, https://doi.org/10.1016/j.carbon.2009.01.009.
[79] D. Graf, F. Molitor, K. Ensslin, C. Stampfer, A. Jungen, C. Hierold, L. Wirtz, Raman imaging of graphene, Solid State Commun. 143 (1-2) (2007) 44–46, https://doi.org/10.1016/j.ssc.2007.01.050.
[80] A.C. Ferrari, J. Robertson, Interpretation of Raman spectra of disordered and amorphous carbon, Phys. Rev. B. 61 (20) (2000) 14095–14107, https://doi.org/10.1103/PhysRevB.61.14095.
[81] W. Xie, L.-T. Weng, K.M. Ng, C.K. Chan, C.-M. Chan, Clean graphene surface through high temperature annealing, Carbon N. Y. 94 (2015) 740–748, https://doi.org/10.1016/j.carbon.2015.07.046.
[82] H. Estrade-Szwarckopf, XPS photoemission in carbonaceous materials: A “defect” peak beside the graphitic asymmetric peak, Carbon N. Y. 42 (8-9) (2004) 1713–1721, https://doi.org/10.1016/j.carbon.2004.03.005.
[83] A. Siokou, F. Ravani, S. Karakalos, O. Frank, M. Kalbac, C. Galiotis, Surface refinement and electronic properties of graphene layers grown on copper substrate: An XPS, UPS and EELS study, Appl. Surf. Sci. 257 (23) (2011) 9785–9790, https://doi.org/10.1016/j.apsusc.2011.06.017.
[84] W. Xie, L.-T. Weng, K.M. Ng, C.K. Chan, C.-M. Chan, Defects of clean graphene and sputtered graphite surfaces characterized by time-of-flight secondary ion mass spectrometry and X-ray photoelectron spectroscopy, Carbon N. Y. 112 (2017) 192–200, https://doi.org/10.1016/j.carbon.2016.11.002.
[85] M. Aliofkhazraei, N. Ali, W.I. Milne, C.S. Ozkan, S. Mitura, J.L. Gervasoni (Eds.), Graphene Science Handbook, CRC Press, 2016. https://doi.org/10.1201/b19460.
[86] P. Patsalas, M. Handrea, S. Logothetidis, M. Gioti, S. Kennou, W. Kautek, A complementary study of bonding and electronic structure of amorphous carbon films by electron spectroscopy and optical techniques, Diam. Relat. Mater. 10 (3-7) (2001) 960–964, https://doi.org/10.1016/S0925-9635(00)00480-5.
[87] A. Nikitin, L.-Å. Näslund, Z. Zhang, A. Nilsson, C-H bond formation at the graphite surface studied with core level spectroscopy, Surf. Sci. 602 (14) (2008) 2575–2580, https://doi.org/10.1016/j.susc.2008.06.012.
[88] H. Kim, I. Song, C. Park, M. Son, M. Hong, Y. Kim, J.S. Kim, H.-J. Shin, J. Baik, H. C. Choi, Copper-Vapor-Assisted Chemical Vapor Deposition for High-Quality and Metal-Free Single-Layer Graphene on Amorphous SiO 2 Substrate, ACS Nano. 7 (8) (2013) 6575–6582, https://doi.org/10.1021/nn402847w.
[89] A.V. Talyzin, S. Luzan, I.V. Anoshkin, A.G. Nasibulin, H. Jiang, E.I. Kauppinen, V. M. Mikoushkin, V.V. Shnitov, D.E. Marchenko, D. Noréus, Hydrogenation, Purification, and Unzipping of Carbon Nanotubes by Reaction with Molecular Hydrogen: Road to Graphane Nanoribbons, ACS Nano. 5 (6) (2011) 5132–5140, https://doi.org/10.1021/nn201224k.
[90] S. Ghosh, K. Ganesan, S.R. Polaki, T.R. Ravindran, N.G. Krishna, M. Kamruddin, A. K. Tyagi, Evolution and defect analysis of vertical graphene nanosheets, J. Raman Spectrosc. 45 (8) (2014) 642–649, https://doi.org/10.1002/jrs.4530.
[91] A.J. Stone, D.J. Wales, Theoretical studies of icosahedral C60 and some related species, Chem. Phys. Lett. 128 (5-6) (1986) 501–503, https://doi.org/10.1016/0009-2614(86)80661-3.
[92] A. Barinov, O.B. Malcioğlu, S. Fabris, T. Sun, L. Gregoratti, M. Dalmiglio, M. Kiskinova, Initial Stages of Oxidation on Graphitic Surfaces: Photoemission Study and Density Functional Theory Calculations, J. Phys. Chem. C. 113 (21) (2009) 9009–9013, https://doi.org/10.1021/jp902051d.
[93] K. Ganesan, S. Ghosh, N. Gopala Krishna, S. Ilango, M. Kamruddin, A.K. Tyagi, A comparative study on defect estimation using XPS and Raman spectroscopy in few layer nanographitic structures, Phys. Chem. Chem. Phys. 18 (32) (2016) 22160–22167, https://doi.org/10.1039/C6CP02033J.
[94] O. Lehtinen, J. Kotakoski, A.V. Krasheninnikov, A. Tolvanen, K. Nordlund, J. Keinonen, Effects of ion bombardment on a two-dimensional target: Atomistic simulations of graphene irradiation, Phys. Rev. B. 81 (2010), 153401, https://doi.org/10.1103/PhysRevB.81.153401.
[95] S.M. Rossnagel, H.R. Kaufman, Current–voltage relations in magnetrons, J. Vac. Sci. Technol. A Vacuum, Surfaces, Film. 6 (2) (1988) 223–229, https://doi.org/10.1116/1.574985.
[96] S.M. Rossnagel, Dynamic interactions in the physical properties of magnetron deposition systems, Mater. Sci. Eng. A. 140 (1991) 510–516, https://doi.org/10.1016/0921-5093(91)90471-X.